

1 **White matter myelination during early infancy is explained by spatial gradients**
2 **and myelin content at birth**

3
4 Mareike Grotheer^{1,2,3*}, Mona Rosenke³, Hua Wu⁴, Holly Kular³, Francesca R. Querdasi³, Vaidehi Natu³, Jason D. Yeatman^{3,5,6,7}, and
5 Kalanit Grill-Spector^{3,5}

6 ¹ Department of Psychology, Philipps-Universität Marburg, Marburg 35039, Germany.

7 ² Center for Mind, Brain and Behavior – CMBB, Philipps-Universität Marburg and Justus-Liebig-Universität Giessen, Marburg 35039,
8 Germany.

9 ³Psychology Department, Stanford University, Stanford, CA 94305, USA.

10 ⁴Cognitive and Neurobiological Imaging Center (CNT), Stanford University, Stanford, CA 94305, USA.

11 ⁵Wu Tsai Neurosciences Institute, Stanford University, CA 94305, USA.

12 ⁶Graduate School of Education, Stanford University, Stanford, CA 94305, USA.

13 ⁷Division of Developmental-Behavioral Pediatrics, Stanford University School of Medicine, Stanford, CA 94305, USA.

14

15 *=corresponding author

16

17

18

19

20

21

22

23

24 **Development of myelin, a fatty sheath that insulates nerve fibers, is critical for brain**
25 **function. Myelination during infancy has been studied with histology, but postmortem data**
26 **cannot evaluate the longitudinal trajectory of white matter development. Here, we obtained**
27 **longitudinal diffusion MRI and quantitative MRI measures of R1 in 0, 3 and 6 months-old**
28 **human infants, and (ii) developed an automated method to identify white matter bundles and**
29 **quantify their properties in each infant’s brain. We find that R1 increases from newborns to 6-**
30 **months-olds in all bundles. R1 development is nonuniform: there is faster development in**
31 **white matter that is less mature in newborns, and along inferior-to-superior as well as anterior-**
32 **to-posterior spatial gradients. As R1 is linearly related to myelin fraction in white matter**
33 **bundles, these findings open new avenues to elucidate typical and atypical white matter**
34 **myelination in early infancy, which has important implications for early identification of**
35 **neurodevelopmental disorders.**

36

37

38

39

40

41

42

43

44

45

46

47 During the first year of life, the volume of the human brain's white matter increases by 6 –
48 16%¹. A key microstructural component of this white matter development is myelination²⁻⁶. That is,
49 the formation of myelin, the fatty sheath that insulates axons that connect different brain regions.
50 Myelin is essential for brain function, as it enables rapid and synchronized neural communication
51 across the brain and abnormalities in myelination are linked to a plethora of developmental and
52 cognitive disorders⁷. However, the principles and nature of white matter myelination of the human
53 brain during early infancy are not well understood.

54 Three main theories of white matter myelin development during infancy have been proposed:
55 1) The starts-first/finishes-first hypothesis, which is based on data from classic histological studies²⁻⁴,
56 proposes that postnatal myelination follows prenatal patterns. This hypothesis predicts that white
57 matter that is more myelinated at birth will develop faster postnatally and will finish myelinating earlier.
58 This, in turn, may allow for most important brain functions to mature the fastest. 2) The speed-up
59 hypothesis, which is based on more recent imaging data^{8,9}, suggests that white matter that is less
60 myelinated at birth develops faster postnatally. This development may be experience-dependent¹⁰⁻¹³
61 and may foster efficient and coordinated transmission of signals across the brain. Both of the above
62 hypotheses build on the observation that myelin content is not homogenous in the newborn brain²⁻
63 ^{5,14}. 3) The spatial-gradient hypothesis suggests that postnatal myelination progresses in a spatially
64 organized manner^{5,15}. Different spatial gradients of myelination have been proposed including that
65 white matter myelination originates in neurons and follows the direction of information flow⁴ or that
66 it occurs along a proximal to distal axis across the brain⁵. It is important to note that, while the starts-
67 first/finishes-first hypothesis and the speed-up hypothesis are mutually exclusive, spatial gradients
68 may contribute to myelination during infancy in addition to the effects of myelin content at birth
69 predicted by the former two hypotheses.

70 Testing these developmental hypotheses requires *in-vivo* measurements of the typical,
71 longitudinal development of myelin along the length of multiple white matter bundles of individual
72 infants. However, classic histological studies compare postmortem brain samples across individuals,

73 often include pathologies, and use observer-dependent methods¹⁶. Thus, classic histology provides a
74 cross-sectional and qualitative glimpse of white matter myelination during infancy. Up to recently^{17–22}
75 most *in vivo* investigations of white matter development leveraged diffusion metrics (e.g., mean
76 diffusivity (MD)), that have a complex, non-linear relationship to myelin and are also affected by other
77 properties of the white matter, including the diameter, spacing, and orientation of fibers^{18,23–25}. Thus,
78 diffusion metrics do not provide accurate measures of myelination. However, quantitative
79 MRI^{9,14,15,18,26–30} (qMRI) measurements, such as the longitudinal relaxation rate, R1 [s⁻¹], now offer
80 metrics that are directly related to myelin content in the white matter. In fact, not only does the amount
81 of myelin in a voxel (myelin fraction) explain 90% of the variance in R1 in white matter bundles^{29,31},
82 but changes in R1 are also linearly related to changes in myelin fraction (**Supplementary Fig 1**). Thus,
83 longitudinal measurements of R1 along white matter bundles enable the assessment of white matter
84 myelin development during infancy.

85 To test the predictions of the developmental hypotheses of white matter myelination during
86 early infancy, we acquired longitudinal measurements of anatomical MRI, diffusion MRI (dMRI), and
87 qMRI in infants during natural sleep at 3 timepoints: newborn (N=9; age: 8-37 days), 3 months (N=10;
88 age: 79-106 days), and 6 months (N=10; age: 167-195 days) of age. We used anatomical MRI to
89 segment the brain to gray and white matter, dMRI to determine the white matter bundles of the infant
90 brain, and qMRI to measure R1 along each WM bundle (**Supplemental Fig 2**). All analyses were
91 performed in infants' native brain space. To relate our findings to prior developmental studies, we
92 also used dMRI data to assess the development of mean diffusivity (MD) in white matter bundles.
93 However, as the relationship between MD and myelin is complex and nonlinear, we cannot accurately
94 estimate from the rate of MD development the rate of myelination⁹.

95 As increases in myelin in the white matter generate linear increases in R1, the developmental
96 hypotheses tested here make the following predictions: The starts-first/finishes-first hypothesis
97 predicts that during the first 6 months of life, R1 will increase faster in white matter that is more
98 myelinated at birth and hence has higher R1 values in newborns. The speed-up hypothesis predicts

99 the opposite, that during the first 6 months of life, R1 will increase faster in white matter that has
100 lower R1 values in newborns. Finally, the spatial gradient hypothesis predicts spatial differences in the
101 development of R1 across the white matter, that cannot be explained by differences in R1 values in
102 newborns.

103

104 **Results**

105 **A new method for automated fiber quantification in babies (babyAFQ)**

106 We first identified each individual infant's white matter bundles in their native brain space in
107 a systematic and automated way. A major challenge is that present automated tools for bundle
108 identification in individuals (e.g. ³²⁻³⁴) have been developed for adults and school-aged children and
109 therefore may not be suitable for infants due to substantial differences in brain size¹ and organization²⁰.
110 Thus, we developed a new pipeline for analyzing infant dMRI data (**Supplementary Fig 2**) and a
111 novel method, baby automated fiber quantification (babyAFQ), for automatically identifying 24
112 bundles (11 in each hemisphere and 2 between-hemispheres, **Supplementary Figs 2-4**) in each
113 individual infant's brain and timepoint (**Supplementary Fig 9**). We optimized babyAFQ for infants
114 by: (i) generating waypoints (anatomical regions of interest (ROIs) for defining bundles) on a newborn
115 brain template (University of North Carolina (UNC) neonatal template³⁵), (ii) decreasing the spatial
116 extent of waypoints compared to adults³⁶ to fit the more compact infant brain, and (iii) adding
117 waypoints for curved bundles to improve their identification.

118 BabyAFQ successfully identifies 24 bundles in each infant and timepoint (example infant: **Fig.**
119 **1**, all infants: **Supplementary Fig 9**), including bundles that have not previously been identified in
120 infants: the posterior arcuate fasciculus³⁷, vertical occipital fasciculus³⁷⁻³⁹, and middle longitudinal
121 fasciculus⁴⁰. The 24 bundles have the expected shape and location in all infants even as their brains
122 grow from 0 to 6 months. 3D interactive visualizations at 0 months
123 (http://vpnl.stanford.edu/babyAFQ/bb11_mri0_interactive.html), 3 months

124 (http://vpnl.stanford.edu/babyAFQ/bb11_mri3_interactive.html) and 6 months of age
 125 (http://vpnl.stanford.edu/babyAFQ/bb11_mri6_interactive.html) show the 3D structure of bundles
 126 in an example infant.

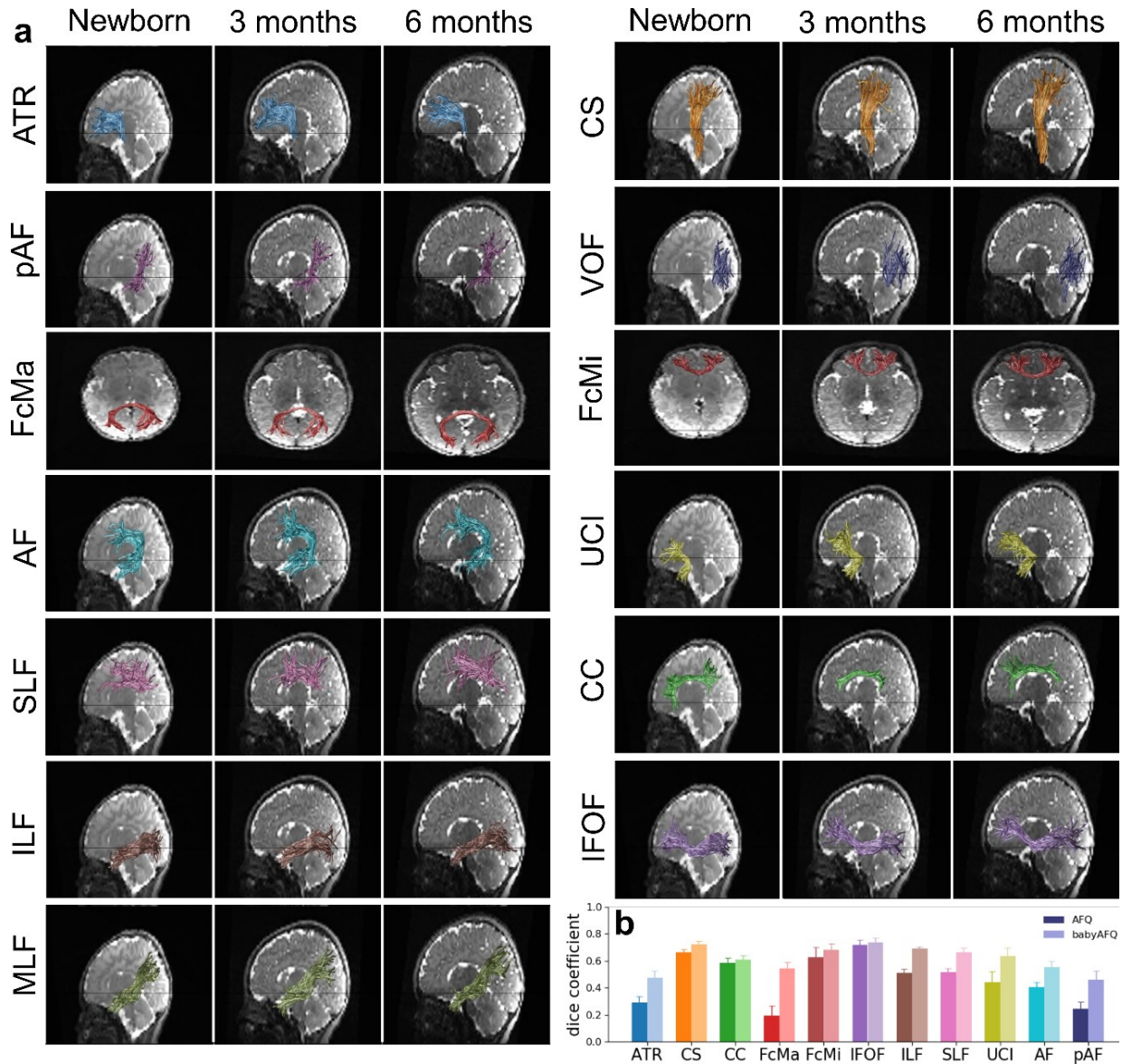


Figure 1. Baby automated fiber quantification (babyAFQ) identifies white matter bundles in individual infant brains across the first 6 months of life. 24 bundles (11 in each hemisphere and 2 cross-hemispheric) were successfully identified in all individuals and ages (**Supplementary Data 3-5**). **a.** All bundles of an individual baby. Each row is a bundle, each column is a timepoint; *left*: newborn, *middle*: 3 months, *right*: 6 months. **b.** Comparison of AFQ and babyAFQ performances in identifying each bundle in newborns relative to manually defined (gold-standard) bundles. Error bars indicate standard error across participants. The dice coefficient quantifies the overlap between the automatically and manually defined bundles, revealing significantly higher performance for babyAFQ than AFQ. *Abbreviations*: ATR: anterior thalamic radiation, CS: cortico-spinal tract, pAF: posterior arcuate fasciculus, VOF: vertical occipital fasciculus, FcMa: forceps major; FcMi: forceps minor, AF: arcuate fasciculus, UCI: uncinata fasciculus, SLF: superior longitudinal fasciculus, CC: cingulum cingulate, ILF: inferior longitudinal fasciculus, IFOF: inferior frontal occipital fasciculus, MLF: middle longitudinal fasciculus.

127 For quality assurance, we compared babyAFQ and AFQ³² (developed in adults and used in
128 prior infant studies⁴¹⁻⁴³) to manually identified bundles (“gold-standard”). In newborns, bundles
129 identified by babyAFQ substantially overlapped the gold-standard (mean dice coefficient \pm standard
130 error (SE): 0.61 \pm 0.02) and this overlap was significantly higher compared to AFQ (**Fig 1b**;
131 **Supplementary Fig 3**; 2-way repeated measure analysis of variance (rmANOVA) with AFQ-type and
132 bundle as factors: AFQ-type: F(1,08)=528.60, p<0.0001, bundle: F(19,152)=11.31, p<0.0001, AFQ-
133 types x bundle: F(19,152)=7.13, p<0.0001; additional 3-way rmANOVA on the 11 bilateral bundles,
134 with AFQ-type, bundle, and hemisphere as factors revealed no effects of, or interaction with,
135 hemisphere). Improvements from babyAFQ were also evident at the other timepoints in qualitative
136 evaluations in individual infants. E.g., the Forceps Major was successfully identified by babyAFQ in
137 29/29 brains, but identified by AFQ in only 13/29 brains.

138

139 **During infancy, R1 increases in all 24 evaluated white matter bundles**

140 We first measured the development of mean R1 in each bundle during the first 6 months of
141 life. Measurements of mean R1 of the 24 bundles identified by babyAFQ at 0, 3, and 6 months reveal
142 a substantial increase in R1 from 0 to 6 months of age (**Fig. 2a**). Mean R1 across bundles \pm SE [range]:
143 0 months: 0.46s⁻¹ \pm 0.007s⁻¹ [0.42-0.55s⁻¹], 3 months: 0.52s⁻¹ \pm 0.008s⁻¹ [0.46-0.63s⁻¹], 6 months: 0.62s⁻¹
144 \pm 0.009s⁻¹ [0.54-0.73 s⁻¹]. This is a profound change, as mean R1 increases on average by ~17% (0.16s⁻¹
145 ¹) within just 6 months. We modeled mean R1 development in each bundle using linear mixed models
146 (LMMs) with age as predictor and a random intercept (estimated R1 at birth) for each participant.
147 Overall, LMMs explained ~90% of the R1 variance across development (adjusted Rs²>0.87,
148 ps<0.0001). As R1 in white matter is linearly related to myelin fraction, these data are consistent with
149 the idea that white matter bundles myelinate during early infancy.

150

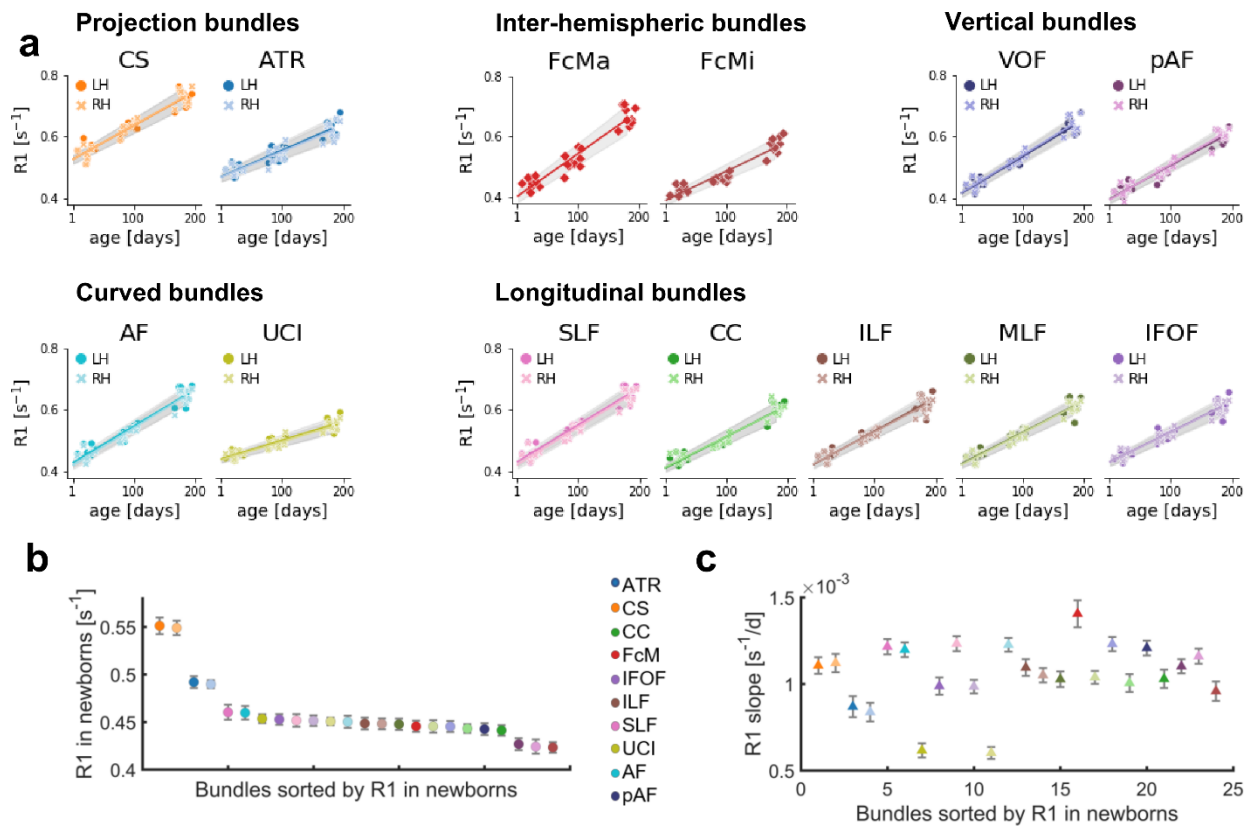


Figure 2. Mean R1 of white matter bundles linearly increases from birth to 6 months of age. **a.** Mean R1 of each bundle as a function of age in days. Each point is a participant; markers indicate hemisphere; lines indicate LMM prediction; lines for both hemispheres fall on top of each other; gray shaded regions indicate 95% confidence intervals. **b.** Mean R1 measured in newborns for 24 white matter bundles; Color: bundle; Darker shades: LH; Error bars: Standard error across participants. **c.** Rate of mean R1 development (slopes from LMMs) during the first 6 months of life for each white matter bundle; Bundles are sorted by R1 at birth and colored as in (b). Error bars: Standard error. *Abbreviations:* CS: cortico-spinal tract, ATR: anterior thalamic radiation, FcMa: forceps major; FcMi: forceps minor, VOF: vertical occipital fasciculus, pAF: posterior arcuate fasciculus, AF: arcuate fasciculus, UCI: uncinate fasciculus, SLF: superior longitudinal fasciculus, CC: cingulum cingulate, ILF: inferior longitudinal fasciculus, MLF: middle longitudinal fasciculus, IFOF: inferior frontal occipital fasciculus, RH: right hemisphere, LH: left hemisphere.

151 To summarize the LMM results we plotted each bundle's mean R1 measured in newborns
 152 (**Fig 2b**) and as its rate of development (**Fig 2c**) with 3 notable findings: (i) Mean R1 measured in
 153 newborns varies across bundles. At birth, projection bundles (CST and ATR) have the highest R1 and
 154 the forceps minor (FMi) and inferior frontal occipital fasciculus (IFOF) have the lowest R1 (**Fig 2b**).
 155 (ii) The rate of R1 development during infancy varies between bundles. Across these 24 bundles, the
 156 Forceps Major (FcMa) has the fastest rate of R1 development, while the Uncinate (UCI) and the
 157 anterior thalamic radiation (ATR) have the slowest rate of R1 development between 0 to 6 months.
 158 (iii) Relating the bundles' rate of R1 development to their R1 measured in newborns reveals no

159 systematic relationship between mean R1 in newborns and rate of mean R1 development (**Fig 2c**).
160 Indeed, there is no significant correlation between R1 in newborns and R1 slopes across bundles
161 ($R^2=0.003$, $p=0.81$). For example, both the cortical spinal tract (CST) and the forceps major (FcMa)
162 have fast R1 development (steep slope) during early infancy, yet they have vastly different mean R1 in
163 newborns. Together, these analyses suggest that mean R1 in newborns does not seem to explain mean
164 R1 development rate during early infancy.

165 To relate our findings to previous work that evaluated diffusion metrics, we also measured the
166 development of mean diffusivity (MD) across bundles. Myelination of the white matter is expected to
167 result in decreases in MD. Consistent with this, we found that mean MD systematically decreases in
168 all 24 white matter bundles during the first 6 months of life (**Supplementary Fig. 5a**). Like R1, mean
169 MD in newborns and the rate of mean MD development varied across bundles (**Supplementary Fig.**
170 **5b,c**). Interestingly, while mean MD and R1 in newborns are correlated ($R^2=0.76$, $p<0.0001$), the rates
171 of MD and R1 development during early infancy are not correlated ($R^2=0.08$, $p=0.17$). That is, the
172 longitudinal developmental patterns observed using MD are different from those observed with R1.
173 For example, the uncinate (UCI) has slow R1 development (shallow slope) but rapid MD development
174 (steep slope). In contrast to R1, we find a negative correlation between the rate of MD development
175 and the measured MD in newborns ($R^2=0.71$, $p<0.0001$), such that bundles with higher mean MD in
176 newborns have an accelerated decrease in MD during early infancy. The differential development of
177 MD and R1 is consistent with prior reports across the lifespan⁴⁴ and suggests that other changes to
178 the white matter beyond myelination contribute to MD development in the first 6 months of life.

179
180 R1 development during early infancy varies along the length of white matter bundles
181 White matter bundles are large structures that span substantial distances across the brain and have
182 variable white matter properties along their length^{32,34,44}. Thus, mean measurements across the entire

183 bundle may not be representative and may even obscure differential development patterns along the
 184 length of the bundles. Thus, we next evaluated R1 development along the length of 24 bundles.

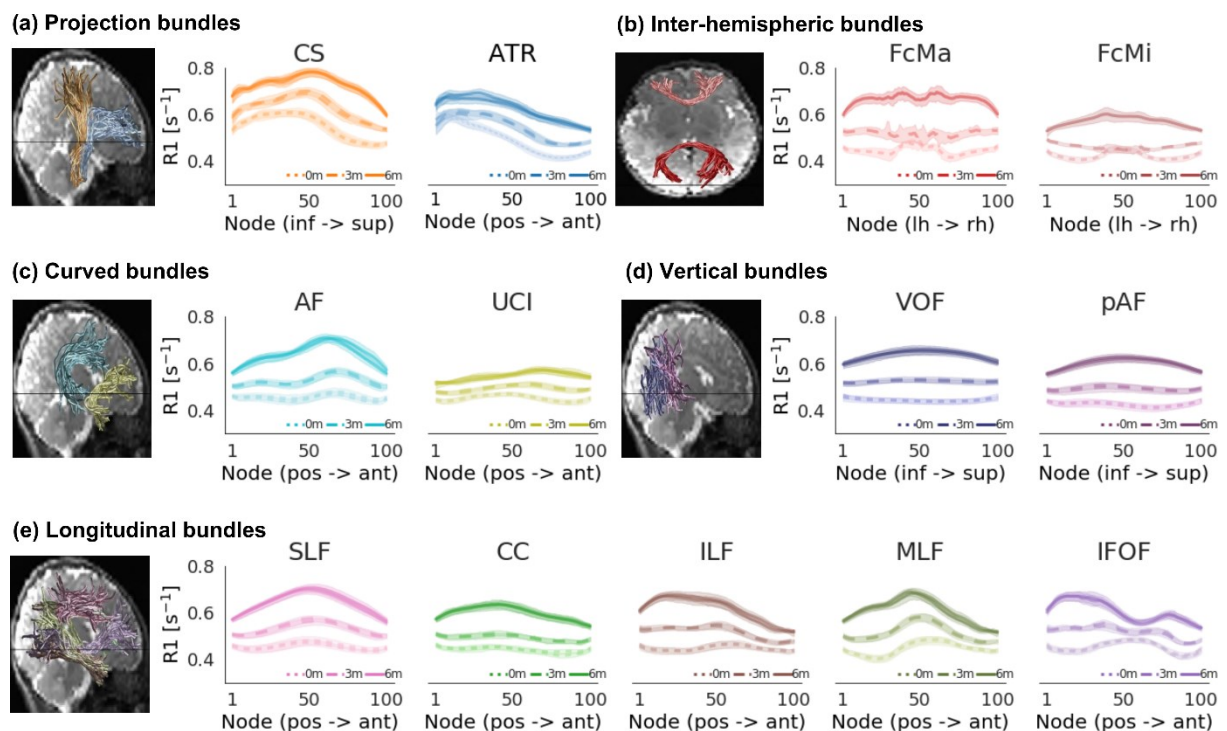


Figure 3. Development of R1 along each bundle. R1 along the length of each bundle in newborns (0m, dotted line), 3-months-olds (3m, dashed line), and 6-months-olds (6m, solid line). *Lines:* average R1 at each node across participants. Lines per hemisphere largely overlap. *Shaded regions:* 95% confidence intervals. Left panels show the bundles in a representative newborn. *Abbreviations:* CS: cortico-spinal tract, ATR: anterior thalamic radiation, FcMa: forceps major; FcMi: forceps minor, VOF: vertical occipital fasciculus, pAF: posterior arcuate fasciculus, AF: arcuate fasciculus, UCI: uncinate fasciculus, SLF: superior longitudinal fasciculus, CC: cingulum cingulate, ILF: inferior longitudinal fasciculus, MLF: middle longitudinal fasciculus, IFOF: inferior frontal occipital fasciculus.

185 We examined the development of R1 along each bundle using babyAFQ with two main
 186 observations: (i) At each timepoint, R1 exhibits spatial variations along the length of these 24 bundles
 187 (**Fig 3**), with the range of variations differing across bundles. For example, the cortico-spinal tract
 188 (CS, **Fig 3a**), exhibits substantial variations in R1 along its length, whereas the vertical occipital
 189 fasciculus (VOF, **Fig 3d**) shows only modest variations. (ii) Consistent with the analyses of mean R1,
 190 along the length of each of these 24 bundles, R1 systematically increases from newborns (**Fig 3-dotted**
 191 **line**), to 3-month-olds (**Fig 3-dashed line**), to 6-months-olds (**Fig 3-solid line**).

192 To quantify R1 development along white matter bundles during the first 6 months of life, we
 193 used LMMs applied independently at 100 equidistant locations (nodes) along each bundle (LMM

194 relating R1 to age; one LMM per node and bundle; random intercepts for individuals). The LMM
 195 slopes estimate the rate of R1 development at each node (**Fig 4-dashed lines**), and we compared the
 196 slope to the measured R1 in newborns at each node (**Fig 4-solid lines**). Results reveals two main
 197 findings: (i) LMM slopes are positive throughout, indicating that R1 increases from birth to 6 months
 198 of age. (ii) In all bundles, there is a nonuniform rate of R1 development along the length of the bundle.
 199 For example, the posterior ends of the inferior longitudinal fasciculus (ILF) and middle longitudinal
 200 fasciculus (MLF) show a larger change in R1 (more positive slope) than their anterior ends (**Fig 4**). As
 201 R1 is linearly related to myelin fraction, these data suggest that myelination occurs at different rates
 202 along the length of these 24 bundles.

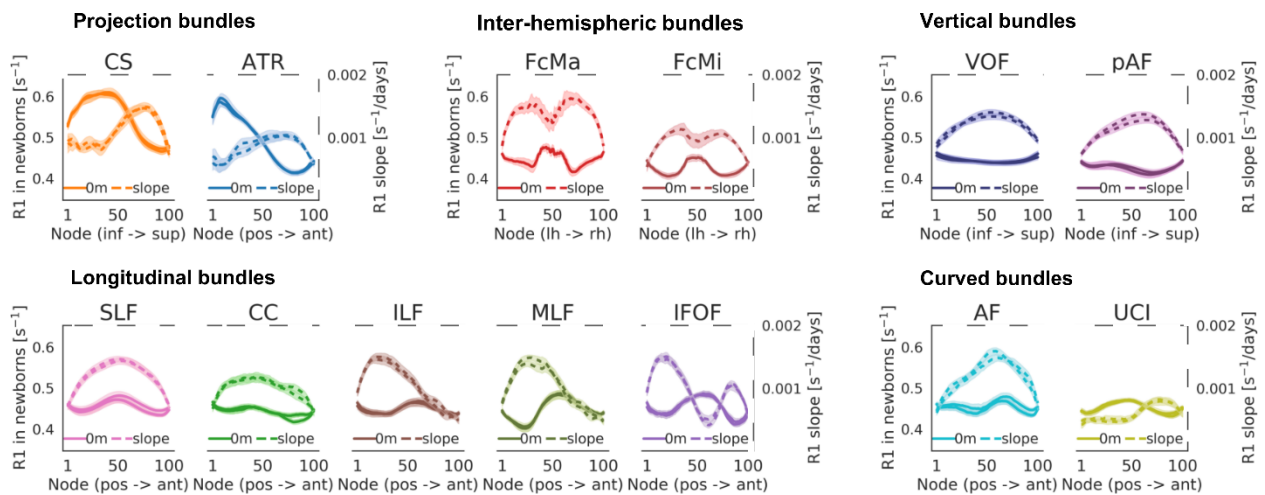


Figure 4. R1 development rate varies along the length of each bundle. a. Each panel jointly shows measured R1 in newborns (left y-axis, solid line) and the slope of R1 development (right y-axis, dashed line) at each node along the bundle. Faster development (more positive slope) corresponds to higher values of dashed lines. Higher R1 in newborns correspond to higher values in solid lines. Lines from both hemispheres are presented separately but fall on top of each other. Shaded regions indicate 95% confidence intervals. *Abbreviations:* CS: cortico-spinal tract, ATR: anterior thalamic radiation, FcMa: forceps major; FcMi: forceps minor, VOF: vertical occipital fasciculus, pAF: posterior arcuate fasciculus, AF: arcuate fasciculus, UCI: uncinata fasciculus, SLF: superior longitudinal fasciculus, CC: cingulum cingulate, ILF: inferior longitudinal fasciculus, MLF: middle longitudinal fasciculus, IFOF: inferior frontal occipital fasciculus.

203 By plotting the rate of R1 development (slopes from LMMs; **Fig 4-dashed**) along each bundle
 204 relative to the measured R1 in newborns (**Fig 4-solid**), we could also begin to assess the three
 205 developmental hypotheses. Results revealed that in some bundles (e.g., the cortico-spinal tract (CS) or
 206 forceps (FcMa/FcMi)) the rate of R1 increase is higher in locations along the bundle where R1 in
 207 newborns is lower. This suggests a negative relationship between R1 development and R1 at birth,

208 consistent with the predictions of the speed-up hypothesis. In other bundles (e.g., posterior acute
209 fasciculus (pAF) or acute fasciculus (AF)), R1 development rate varies substantially along the length
210 of the bundle, but not in a clear relation to R1 measured in newborns. This is consistent with the
211 predictions of the spatial gradient hypothesis. These qualitative observations provide first evidence
212 that multiple factors including spatial gradients and R1 at birth may contribute to the development of
213 R1 along white matter bundles.

214 Like R1, MD shows (i) spatial variations along the length of each of these 24 bundles at all
215 three time-points, and (ii) significant development along the length of each bundle (**Supplementary**
216 **Fig. 6**). Different than R1, (i) MD decreases with age (**Supplementary Fig. 6**), and (ii) the rate of
217 MD development along the bundles shows a spatially distinct pattern compared to R1
218 (**Supplementary Figure 7**). This analysis provides additional evidence that development of MD in
219 white matter bundles differs from R1 during early infancy.

220

221 **Spatial gradients and R1 at birth together explain R1 development**

222 The prior visualizations of R1 along white matter bundles suggest that both R1 at birth and
223 the spatial location in the brain may contribute to the rate of R1 development during early infancy. To
224 gain a global understanding of the spatial nature of R1 development across the white matter of the
225 human brain, next, we visualized R1 measured in newborns and the rate of R1 development of white
226 matter bundles in the 3D brain space of newborns (plotting every 10th node, **Fig 5**), rather than along
227 each individual bundle (as in **Figs 3,4**). These 3D visualizations yield the following observations: (i)
228 R1 in newborns varies spatially across the brain with overall highest values in central white matter and
229 lowest values in frontal white matter (**Fig 5b**), and (ii) the rate of R1 development varies spatially
230 across the brain with faster increases in occipital and parietal white matter (yellow in **Fig 5c**) and
231 slower development in the temporal and frontal white matter (black in **Fig 5c**). Overall, these
232 visualizations suggest that both R1 at birth and spatial gradients across the brain appear to contribute
233 to the rate of R1 development during early infancy. Thus, we next quantitatively tested the significance

234 of each of these two factors separately, and then tested the viability of a model incorporating both
 235 factors. We applied a similar approach to MD (**Supplementary Fig. 8**).

236 First, we tested if the rate of R1 development is related to R1 measured in newborns (LMM
 237 relating R1 slope to R1 measured in newborns at every 10th node, with a random intercept per bundle).
 238 The speed up hypothesis predicts a significant negative relationship but the starts-first/finishes-first
 239 hypothesis predicts a significant positive relationship. LMM results reveal a significant negative
 240 relationship between the rate of R1 development and R1 measured in newborns across the white
 241 matter ($\beta=-0.003$, $p<0.0001$), that accounts for 40% of the variance in R1 slopes ($R^2=0.40$). That is,
 242 nodes that have higher R1 in newborns develop more slowly than nodes that have lower R1 in
 243 newborns, which is consistent with the speed-up hypothesis.

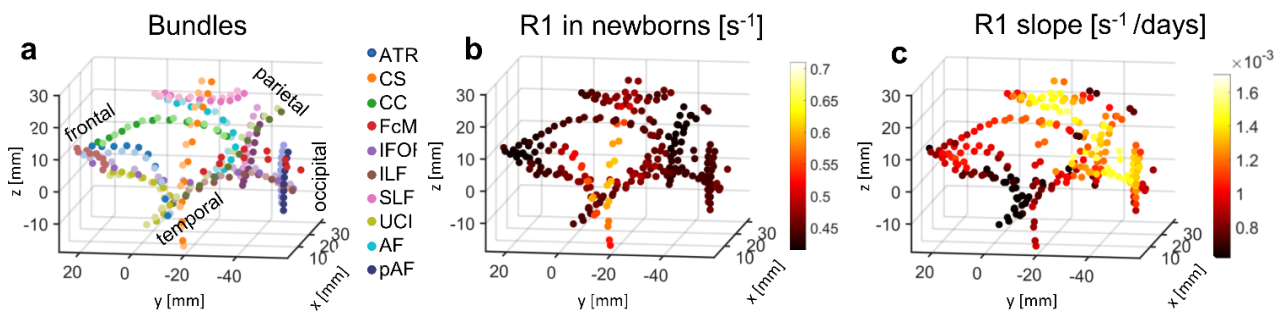


Figure 5. Spatial gradients and R1 at birth together explain R1 development. In all panels each point is a node. In all plots only every 10th node of a bundle is plotted to ensure spatial independence of tested nodes. The coordinate of each node is the average $|x|, y, z$ coordinate across newborns. As all data was acpc-ed, the 0,0,0 coordinate is the anterior commissure; $|x|$ -axis is medial to lateral; y-axis is posterior to anterior; z-axis is inferior to superior. The axes are identical across panels. (a) 3D spatial layout of the 24 bundles in the average newborn brain volume. Nodes are color coded by bundle (see legend); approximate lobe annotations are included to clarify the spatial layout. (b) 3D spatial layout of measured R1 at each node in newborns [s⁻¹]. Data are averaged across participants. Color indicates R1. (c) 3D spatial layout of R1 development rate [s⁻¹/day] (i.e. the slope estimated from LMM) at each node. *Abbreviations:* CS: cortico-spinal tract, ATR: anterior thalamic radiation, FcMa: forceps major; FcMi: forceps minor, VOF: vertical occipital fasciculus, pAF: posterior arcuate fasciculus, AF: arcuate fasciculus, UCI: uncinate fasciculus, SLF: superior longitudinal fasciculus, CC: cingulum cingulate, ILF: inferior longitudinal fasciculus, MLF: middle longitudinal fasciculus, IFOF: inferior frontal occipital fasciculus.

244 Second, we tested the spatial gradient hypothesis and evaluated if the rate of R1 development
 245 at each node is related to its spatial location in the brain (LMM relating R1 slope at every 10th node to
 246 the nodes average coordinates in newborns $|x|, y, z$, and their interactions $|x|*y, |x|*z$, and $z*y$;
 247 random intercept per bundle). Results show that there is a significant relationship between the rate of

248 R1 development and spatial location along the z and y axes and their combination (z: $\beta=1.68*10^{-4}$,
249 $p<0.0001$, y: $\beta=-1.10*10^{-4}$, $p<0.0001$, y*z: $\beta=1.05*10^{-4}$, $p<0.0001$), and smaller but significant
250 relationships along the |x| and |x|*y axes (x: $\beta=4.19*10^{-5}$, $p=0.02$, |x|*y: $\beta=-4.74*10^{-5}$, $p=0.03$),
251 which together explain 65% of the variance ($R^2=0.65$). These results support the spatial gradient
252 hypothesis and suggest that the prominent spatial gradients of development during infancy are from
253 inferior to superior, and from anterior to posterior, with additional gradients along medial to lateral
254 directions.

255 As both R1 measured in newborns and spatial gradients explain a considerable amount of
256 variance, a question remains if they are independent factors contributing to the rate of R1 development
257 or not. Thus, we tested if the rate of R1 development at a node depends both on its spatial location
258 and its R1 measured in newborns (LMM relating R1 slope at every 10th node to measured R1 in
259 newborns and spatial coordinate: |x|, y, z, |x|*y, |x|*z, and z*y; with a random intercept per bundle).
260 This combined model showed a significant negative relationship between the rate of R1 development
261 and R1 measured in newborns: ($\beta =-0.001$; $p=0.002$) and significant effects of spatial location along
262 the z axis ($\beta=1.53*10^{-4}$, $p<0.0001$), y-axis ($\beta=-1.11*10^{-4}$, $p<0.0001$), y*z axis ($\beta=1.04*10^{-4}$, $p<0.0001$),
263 and |x|*z axis ($\beta=3.50*10^{-5}$, $p=0.03$). Overall, this combined model explains 67% of the variance in
264 the rate of R1 development ($R^2=0.67$) and outperforms the best individual model, which was the
265 spatial gradient model (likelihood ratio test, $p=0.002$). Similarly, we find that both MD measured in
266 newborns and spatial gradients explain the rate of MD development in the white matter
267 (**Supplementary Fig. 8**).

268 These analyses suggest that the nonuniform rate of R1 development across the white matter
269 during early infancy can be explained by two factors: initial R1 (measured in newborns) and spatial
270 location in the brain (particularly along the inferior-to-superior and anterior-to-posterior axes).

271

272

273 Discussion

274 By combining longitudinal measures of diffusion MRI and quantitative MRI with a novel
275 approach for automatic bundle quantification (babyAFQ) in individual infant's brains, we evaluated
276 the longitudinal development of R1 and MD during early infancy along 24 white matter bundles, with
277 three main findings: First, in accordance with previous work¹⁵, we find that across the white matter
278 R1 systematically increases from newborns to 6-months-olds. Second, we find that the development
279 of R1 is nonuniform across the white matter. Third, we discovered that the rate of R1 development
280 during infancy is explained by both R1 at birth and spatial gradients. As R1 develops faster in sections
281 of bundles that are less mature in newborns and it is linearly related to myelin, these data support the
282 speed-up hypothesis of infant myelin development. Additionally, the rate of R1 development increases
283 along the inferior-to-superior axis, the anterior-to-posterior axis as well as along diagonal axes. These
284 data suggest that myelination of the white matter during early infancy depends both on the initial
285 myelin content at birth and spatial gradients.

286 Interestingly, the observed developmental pattern of MD showed both similarities and
287 differences from developmental pattern of R1. Consistent with the notion that increases in myelin
288 (and R1) would be associated with decreases in MD, we find that MD in the white matter decreases
289 during infancy, as reported previously⁴⁵⁻⁴⁷. However, we also find that the rate and pattern of MD and
290 R1 development across the white matter are not identical. As MD is impacted by structural
291 components of the white matter beyond myelin (e.g., fiber diameter and packing^{18,23-25}) these
292 differences (i) highlight the importance of using measures such as R1 which are linearly related to
293 myelin^{26,29-31} to assess myelin development specifically, and (ii) suggest that additional properties of
294 white matter bundles beyond myelin are also developing during early infancy. Future histological
295 measurements in postmortem pediatric samples may elucidate these mechanisms.

296 Crucially, as quantitative R1 measures are comparable across MRI scanners of the same field
297 strength^{9,15,26}, we can compare our R1 measurements in infants to those of other populations. For
298 example, we find that R1 in white matter bundles of full-term newborns ranges between 0.42-0.55[s

299 ¹], which is higher than R1 in the white matter of preterm newborns, which ranges between 0.29-
300 0.36[s⁻¹]⁴⁸. This observation suggests that at birth there is some level of myelin in all 24 bundles
301 investigated here, contrasting with classic histological studies which reported myelin only in a handful
302 of white matter bundles in newborns (e.g., the cortical-spinal tract)²⁻⁵. As these classic studies used
303 qualitative visual inspection of myelin stains, rather than quantitative metrics, our data underscore the
304 utility of quantitative R1 measurements. Our measurements also reveal that R1 in 6-months-olds'
305 bundles ranges between 0.54-0.73[s⁻¹], which is lower than the average R1 measured in adults' bundles,
306 which ranges between 0.80-1.25[s⁻¹]^{44,49}. This comparison suggests that none of the 24 bundles
307 investigated here are fully myelinated by 6 months of age. This is not surprising, as the average R1
308 across the white matter develops roughly linearly during the first year of life, after which development
309 slows down¹⁵, but continues until early adulthood^{44,50}. It is interesting that the bundles' R1 increases
310 on average by ~17% (0.16[s⁻¹]) within the first 6 months of life, as this change is larger than the increase
311 of ~0.05[s⁻¹] observed over 10 years of childhood development⁴⁴ (from 8 to 18 years-old). This
312 observation highlights the profound changes occurring in the white matter during early infancy.

313 The finding that less mature white matter at birth myelinates faster during infancy is important
314 for several reasons. First, our data not only provides empirical evidence against the classic view that
315 white matter develops in a strictly hierarchically manner from early sensory to higher-level cognitive
316 regions^{2,3}, but also offers new insights regarding the nature of white matter development in infancy.
317 As myelination is experience-dependent¹⁰⁻¹³, and we find that the rate of myelination after birth is
318 negatively related to its initial (birth) level, one conjecture from our data is that the postnatal
319 environment and experiences may produce a flurry of myelination during the first 6 months of life,
320 overtaking earlier prenatal gradients. Second, as previous data has shown a link between cognitive
321 development, processing speed and myelin development during infancy and early childhood^{51,52}, we
322 further hypothesize that the observed negative relationship between myelination at birth and the rate
323 of myelin development is functionally relevant. For example, one consequence of this developmental

324 trajectory is that it generates a more uniform distribution of myelin across the white matter, which
325 may allow more coordinated and efficient communication across the human brain.

326 The rate of R1 development also varies spatially, with faster development occurring
327 prominently in the inferior-to-superior and anterior-to-posterior directions. As a result of these spatial
328 gradients, white matter that falls within the parietal and occipital lobes develops faster than central,
329 frontal, and temporal white matter. This spatial pattern differs from observations made in preterm
330 newborns before 40 weeks of gestation, that showed fastest development in the central white matter⁴⁸.
331 Instead, this pattern is more aligned with spatial gradients observed later in infancy and early
332 childhood¹⁵. An open question is whether these spatial gradients are innate, or experience driven. One
333 interesting avenue to answer this question in future research would be to compare the longitudinal
334 development of spatial gradients across preterm newborns and full-term newborns. We hypothesize
335 that the consequence of these spatial gradients may be to allow white matter that supports crucial
336 functions such as vision (occipital lobe) and motor control (parietal lobe) to develop faster during
337 infancy.

338 Finally, our study has important societal implications. First, as R1 values are quantitative and
339 have units that can be numerically compared across scanners, populations, and individuals²⁶, our
340 measurements in typically-developing infants provide a key foundation for large-scale studies of infant
341 brain development in typical^{53,54} and clinical populations such as preterm infants⁵⁵, infants with
342 cerebral palsy⁵⁶, or fetal alcohol spectrum disorders⁵⁷. Second, our methodology is translatable to
343 clinical settings as it is performed during natural sleep. Third, we developed an automated processing
344 pipeline that simultaneously provides high throughput and high precision in individual infants. This
345 level of precision may enable early identification of developmental impairments in at-risk infants,
346 which in turn may improve the efficacy of interventions⁵⁸. Further, the spatial precision awarded by
347 our methods may facilitate future work on spatial dependency of both quantitative and diffusion
348 metrics. For example, it would be interesting to formally assess if and how these measures change in
349 spatial locations where multiple bundles cross each other.

350 In conclusion, we find that during early infancy myelin content at birth and spatial gradients
351 of myelin development together explain the rate of myelin growth across the white matter of the
352 human brain. This finding offers a new parsimonious model of white matter development during early
353 infancy. We hypothesize that this pattern of myelination during infancy enables some level of myelin
354 becoming quickly available throughout the brain, to promote efficient and coordinated
355 communication across the brain, while at the same time prioritizing the development of most critical
356 functions such as vision and motor coordination.

357

358 **Methods**

359 **Participants**

360 16 full-term and healthy infants (7 female) were recruited to participate in this study. Three
361 infants provided no usable data because they could not stay asleep once the MRI sequences started
362 and hence, we report data from 13 infants (6 female) across three timepoints: newborn (N=9; age: 8-
363 37 days), 3 months (N=10; age: 79-106 days), and 6 months (N=10; age: 167-195 days). Two
364 participants were re-invited to complete scans for their 6-months session that could not be completed
365 during the first try. Both rescans were performed within 7 days and participants were still within age
366 range for the 6-months timepoint. The participant population was racially and ethnically diverse
367 reflecting the population of the Bay Area, including two Hispanic, nine Caucasian, two Asian, and
368 three multiracial participants. Six out of the 13 infants participated in MRI in all three timepoints (0,
369 3, 6 months). Due to the Covid-19 pandemic and restricted research guidelines, data acquisition was
370 halted. Consequently, the remaining infants participated in either 1 or 2 sessions.

371 Expectant mothers and their infants in our study were recruited from the San Francisco Bay
372 Area using social media platforms. We performed a two-step screening process for expectant mothers.
373 First, mothers were screened over the phone for eligibility based on exclusionary criteria designed to
374 recruit a sample of typically developing infants and second, eligible expectant mothers were screened

375 once again after giving birth. Exclusionary criteria for expectant mothers were as follows: recreational
376 drug use during pregnancy, significant alcohol use during pregnancy (more than 3 instances of alcohol
377 consumption per trimester; more than 1 drink per occasion), lifetime diagnosis of autism spectrum
378 disorder or a disorder involving psychosis or mania, taking prescription medications for any of these
379 disorders during pregnancy, insufficient written and spoken English ability to understand the
380 instructions of the study, or learning disabilities that would preclude participation in the study.
381 Exclusionary criteria for infants were: preterm birth (<37 gestational weeks), low birthweight (<5 lbs
382 8 oz), small height (<18 inches), any congenital, genetic, and neurological disorders, visual problems,
383 complications during birth that involved the infant (e.g., NICU stay), history of head trauma, and
384 contraindications for MRI (e.g., metal implants). Study protocols for these scans were approved by
385 the Stanford University Internal Review Board on Human Subjects Research. Participants were
386 compensated for their participation in the study.

387

388 **Data Acquisition Procedure**

389 Data collection procedure was developed in a recent study⁵⁹. All included participants
390 completed the multiple scanning protocols needed to obtain anatomical MRI, qMRI, and dMRI data.
391 Data were acquired at two identical 3T GE Discovery MR750 Scanners (GE Healthcare) with Nova
392 32-channel head coils (Nova Medical) located at Stanford University: (i) Center for Cognitive and
393 Neurobiological Imaging (CNI) and (ii) Lucas Imaging Center. As infants have low weight, all imaging
394 was done with first level SAR to ensure their safety.

395 Scanning sessions were scheduled in the evenings close in time to the infants' typical bedtime.
396 Each session lasted between 2.5 – 5 hours including time to prepare the infant and waiting time for
397 them to fall asleep. Upon arrival, caregivers provided written, informed consent for themselves and
398 their infant to participate in the study. Before entering the MRI suite, both caregiver and infant were
399 checked to ensure that they were metal-free, and caregivers changed the infant into MR safe cotton
400 onesies and footed pants provided by the researchers. The infant was swaddled with a blanket with

401 their hands to their sides to avoid their hands creating a loop. During sessions involving newborn
402 infants, an MR safe plastic immobilizer (MedVac, www.supertechx-ray.com) was used to stabilize the
403 infant and their head position. Once the infant was ready for scanning, the caregiver and infant entered
404 the MR suite. The caregiver was instructed to follow their child's typical sleep routine. As the infant
405 was falling asleep, researchers inserted soft wax earplugs into the infant's ears. Once the infant was
406 asleep, the caregiver was instructed to gently place the infant on a makeshift cradle on the scanner
407 bed, created by weighted bags placed at the edges of the bed to prevent any side-to-side movement.
408 Finally, to lower sound transmission, MRI compatible neonatal Noise Attenuators
409 ([https://newborncare.natus.com/products-services/newborn-care-products/nursery-](https://newborncare.natus.com/products-services/newborn-care-products/nursery-essentials/minimuffs-neonatal-noise-attenuators)
410 [essentials/minimuffs-neonatal-noise-attenuators](https://newborncare.natus.com/products-services/newborn-care-products/nursery-essentials/minimuffs-neonatal-noise-attenuators)) were placed on the infant's ears and additional pads
411 were also placed around the infant's head to stabilize head position.

412 An experimenter stayed inside the MR suite with the infant during the entire scan. For
413 additional monitoring of the infant's safety and tracking of the infant's head motion, an infrared
414 camera was affixed to the head coil and positioned for viewing the infant's face in the scanner. The
415 researcher operating the scanner monitored the infant via the camera feed, which allowed for the scan
416 to be stopped immediately if the infant showed signs of waking or distress. This setup also allowed
417 tracking the infant's motion; scans were stopped and repeated if there was excessive head motion. To
418 ensure scan data quality, in addition to real-time monitoring of the infant's motion via an infrared
419 camera, MR brain image quality was also assessed immediately after acquisition of each sequence and
420 sequences were repeated if necessary.

421

422 **Data Acquisition Parameters and Preprocessing**

423 Anatomical MRI: T2-weighted images were acquired and used for tissue segmentations. T2-
424 weighted image acquisition parameters: TE=124 ms; TR = 3650ms; echo train length = 120; voxel size
425 = 0.8mm³; FOV=20.5cm; Scan time: 4 min and 5 sec.

426 We generated gray/white matter tissue segmentations of all infants and time-points and used
427 these segmentations to optimize tractography (anatomically constrained tractography, ACT⁶⁰). The
428 T2-weighted anatomy, and a synthetic T1-weighted whole brain image generated from the SPGRs and
429 IR-EPI scans using mrQ software (<https://github.com/mezera/mrQ>) were aligned and used for
430 segmentations. Multiple steps were applied to generate accurate segmentations of each infant's brain
431 at each timepoint⁵⁹. (1) An initial segmentation of gray and white matter was generated from the T1-
432 weighted brain volume using infant FreeSurfer's automatic segmentation code (infant-recon-all;
433 <https://surfer.nmr.mgh.harvard.edu/fswiki/infantFS⁶¹>). (2) A second segmentation was done using
434 the T2-weighted anatomical images, which have a better contrast between gray and white matter in
435 young infants, using the brain extraction toolbox (Brain Extraction and Analysis Toolbox, iBEAT,
436 v:2.0 cloud processing, <https://ibeat.wildapricot.org/⁶²⁻⁶⁴>). (3) The iBEAT segmentation, that was
437 more accurate, was manually corrected to fix segmentation errors (such as holes and handles) using
438 ITK-SNAP (<http://www.itksnap.org/>). (4) The iBEAT segmentation was then reinstalled into
439 FreeSurfer and the resulting segmentation in typical FreeSurfer format was used to optimize
440 tractography.

441
442 Quantitative MRI: An inversion-recovery EPI (IR-EPI) sequence was used to estimate
443 relaxation time (R1) at each voxel. Spoiled-gradient echo images (SPGRs) were used together with the
444 EPI sequence to generate whole-brain synthetic T1-weighted images. We acquired 4 SPGRs whole
445 brain images with different flip angles: $\alpha = 4^\circ, 10^\circ, 15^\circ, 20^\circ$; TE=3ms; TR =14ms; voxel size=1mm³;
446 number of slices=120; FOV=22.4cm; Scan time: 4 times ~5 minutes. We also acquired multiple
447 inversion times (TI) in the IR-EPI using a slice-shuffling technique⁶⁵: 20 TIs with the first TI=50ms
448 and TI interval=150ms as well as a second IR-EPI with reverse phase encoding direction. Other
449 acquisition parameters were: voxel size=2mm³; number of slices=60; FOV=20cm; in-plane/through-
450 plane acceleration=1/3; Scan time=two times 1:45 min.

451 IR-EPI data were used to estimate R1 ($R1=1/T1$) at each voxel. First, as part of the
452 preprocessing, we performed susceptibility-induced distortion correction on the IR-EPI images using
453 FSL's top-up and the IR-EPI acquisition with reverse phase encoding direction. We then used the
454 distortion corrected images to fit the T1 relaxation signal model using a multi-dimensional Levenberg-
455 Marquardt algorithm⁶⁶. The signal equation of T1 relaxation of an inversion-recovery sequence is an
456 exponential decay:

$$457 \quad S(t) = a(1 - be^{-t/T1}),$$

458 where t is the inversion time, a is proportional to the initial magnetization of the voxel, b is
459 the effective inversion coefficient of the voxel (for perfect inversion $b=2$). We applied an absolute
460 value operation on both sides of the equation and used the resulting equation as the fitting model. We
461 use the absolute value of the signal equation because we use the magnitude images to fit the model.
462 The magnitude images only keep the information about the strength of the signal but not the phase
463 or the sign of the signal. The output of the algorithm is the estimated T1 in each voxel. From the T1
464 estimate we calculated R1 ($R1=1/T1$) at each voxel.

465
466 Diffusion MRI: We obtained dMRI data with the following parameters: multi-shell, #diffusion
467 directions/b-value = 9/0, 30/700, 64/2000; TE = 75.7 ms; TR=2800ms; voxel size = 2mm³; number
468 of slices=60; FOV=20cm; in-plane/through-plane acceleration = 1/3; scan time: 5:08 min. We also
469 acquired a short dMRI scan with reverse phase encoding direction and only 6 b=0 images (scan time
470 0:20 min).

471 dMRI preprocessing was performed in accordance with recent work from the developing
472 human connectome project^{67,68}, using a combination of tools from MRtrix3^{69,70}
473 (github.com/MRtrix3/mrtrix3) and mrDiffusion (<http://github.com/vistalab/vistasoft>). We (i)
474 denoised the data using a principal component analysis⁷¹, (ii) used FSL's top-up tool
475 (<https://fsl.fmrib.ox.ac.uk/>) and one image collected in the opposite phase-encoding direction to

476 correct for susceptibility-induced distortions, (iii) used FSL's eddy to perform eddy current and motion
477 correction, whereby motion correction included outlier slice detection and replacement⁷², and (iv)
478 performed bias correction using ANTs⁷³. The preprocessed dMRI images were registered to the
479 whole-brain T2-weighted anatomy using whole-brain rigid-body registration and alignment quality was
480 checked for all images. dMRI quality assurance was also performed. Across all acquisitions, less than
481 $5\% \pm 0.72\%$ of dMRI images were identified as outliers by FSL's eddy tool. We found no significant
482 effect of age across the outliers (no main effect of age: $F(2,26)=1.97$, $p=0.16$, newborn: $1.07+0.88\%$;
483 3 months: $0.4+0.40\%$; 6 months: $0.67+0.85\%$), suggesting that the developmental data was well
484 controlled across all time-points.

485 Next, voxel-wise fiber orientation distributions (FODs) were calculated using constrained
486 spherical deconvolution (CSD) in MRtrix3⁶⁹ (**Supplementary Figure 2**). We used the Dhollander
487 algorithm⁷⁴ to estimate the three-tissue response function, and we lowered the FA threshold to 0.1 to
488 account for the generally lower FA in infant brains. We computed FODs with multi-shell multi-tissue
489 CSD⁷⁵ separately for the white matter and the CSF. As in previous work⁶⁷, the gray matter was not
490 modeled separately, as white and gray matter do not have sufficiently distinct b-value dependencies to
491 allow for a clean separation of the signals. Finally, we performed multi-tissue informed log-domain
492 intensity normalization.

493 We used MRtrix3⁶⁹ to generate a whole brain white matter connectome for each infant and
494 time point. Tractography was optimized using the tissue segmentation from the anatomical MRI data
495 (anatomically-constrained tractography, ACT⁶⁰). We argue that this approach is particularly useful for
496 infant data, as gray and white matter cannot be separated in the FODs. For each connectome, we used
497 probabilistic fiber tracking with the following parameters: algorithm: IFOD1, step size: 0.2 mm,
498 minimum length: 4 mm, maximum length: 200 mm, FOD amplitude stopping criterion: 0.05,
499 maximum angle: 15° . Seeds for tractography were randomly placed within the gray/white matter
500 interface (from anatomical tissue segmentation), which enabled us to ensure that tracts reach the gray

501 matter. Each connectome consisted of 2 million streamlines. MRtrix3 software was also used to fit
502 tensor kurtosis models from which we estimated mean diffusivity (MD) maps for each individual.

503

504 **Bundle delineation with baby automated fiber quantification (babyAFQ)**

505 Here we developed a new toolbox (babyAFQ) that identifies white matter bundles in
506 individual infants. BabyAFQ is openly available as a novel component of AFQ³²
507 (<https://github.com/yeatmanlab/AFQ/tree/master/babyAFQ>) and identifies the following bundles
508 in infants (**Fig. 1**): anterior thalamic radiation (ATR), cortico-spinal tract (CS), posterior arcuate
509 fasciculus (pAF), vertical occipital fasciculus (VOF), forceps major (FcMa), forceps minor (FcMi),
510 arcuate fasciculus (AF), uncinate fasciculus (UCI), superior longitudinal fasciculus (SLF), cingulum
511 cingulate (CC), inferior longitudinal fasciculus (ILF), inferior frontal occipital fasciculus (IFOF) and
512 the middle longitudinal fasciculus (MLF).

513 BabyAFQ uses anatomical ROIs as waypoints for each bundle. That is, a given tract is
514 considered a candidate for belonging to a bundle only if it passes through all waypoints associated
515 with that bundle. The waypoint ROIs were adjusted from those commonly used in adults³⁶ to better
516 match the head size and white matter organization of infants (**Supplementary Fig 3**). Specifically,
517 we: (i) spatially restricted some of the waypoint ROIs to account for the more compact infant brain,
518 (ii) introduced a third waypoint for curvy bundles, (iii) as the VOF was the only bundle that used
519 cortical-surface waypoint ROIs, we generated new volumetric waypoint ROIs for the VOF
520 (**Supplementary Figure 4**), so that all waypoints for all bundles are volumetric, and (iv) added new
521 waypoint ROIs for identifying the MLF, as the MLF was not included in prior AFQ versions.
522 Critically, these waypoints were defined in a neonate infant template brain (UNC Neonatal template³⁵)
523 and are transformed from this template space to each individual infant's brain space before bundle
524 delineation. The use of an infant template brain is critical as commonly used adult templates, such as
525 the MNI brain, are substantially larger and difficult to align to infants' brains. In cases where a given
526 tract is a candidate for multiple bundles, a probabilistic atlas, which is also transformed from the infant

527 template space to the individual infant brain space, is used to determine which bundle is the better
528 match for the tract. Bundles are then cleaned by removing tracts that exceed a gaussian distance of 4
529 standard deviations from the core of the bundle. Critically, babyAFQ was designed to seamlessly
530 integrate with AFQ, so that additional tools for plotting, tract profile evaluation and statistical analysis
531 can be applied after bundle delineation.

532

533 **BabyAFQ quality assurance**

534 To evaluate the quality of the bundle delineation by babyAFQ, we compared the automatically
535 identified bundles to manually delineated “gold-standard” bundles. Manual bundle delineation was
536 performed for the newborns in DSI Studio (<http://dsi-studio.labsolver.org/>) by 2 anatomical experts
537 who were blind to the results of babyAFQ. As a benchmark, we also delineated bundles with AFQ,
538 which was developed using adult data, and compared these bundles to the “gold-standard” bundles.
539 For both babyAFQ and AFQ we quantified the spatial overlap between the automatically identified
540 bundles and the manually identified bundles using the dice coefficient⁷⁶ (DC): $DC = \frac{2|A \cap B|}{|A| + |B|}$, where
541 $|A|$ are voxels of automatically-identified bundles, $|B|$ are voxels of the manual bundles, and $|A \cap B|$
542 is the intersection between these two sets of voxels (**Fig 1b**). We compared dice coefficients between
543 babyAFQ and AFQ in two repeated measures analyses of variance (rmANOVAs). First, a 2-way
544 rmANOVA with AFQ-type and bundle as factors allowed us to evaluate the effect of AFQ type across
545 all bundles. Second, a 3-way rmANOVA with AFQ-type, bundle, and hemisphere as factors, that only
546 included bilateral bundles, enabled us to test for additional hemispheric differences. Finally, we also
547 used the dice coefficients to test if tracts identified as belonging to the VOF were similar or different
548 across methods – using volumetric way-point ROIs vs. surface ROIs (**Supplementary Fig 4**).

549 In addition to the quantitative evaluation, we examined all bundles delineated using babyAFQ
550 and AFQ qualitatively at all time-points (**Supplementary Fig 9**) to evaluate how well they match the

551 typical spatial extent and trajectory across the brain. We also created with pyAFQ³⁴ an interactive 3D
552 visualization of an example infant's bundles at each time point: [0 months](#), [3 months](#), and [6 months](#).

553

554 **Modeling R1 development**

555 After identifying all bundles with babyAFQ, we modeled their R1 development using linear
556 mixed models (LMMs). First, we modeled mean R1 development within each bundle using LMMs
557 with age as predictor and a random intercept (estimated R1 at birth) for each individual (**Fig 2a**). We
558 used model comparison (likelihood ratio tests) to determine that LMMs allowing different slopes for
559 each individual do not better explain the data compared to LMMs using a single slope across
560 individuals. To evaluate differences in developmental trajectories between bundles, we plotted the
561 mean R1 measured in newborns (**Fig 2b**) and well as the mean R1 development rate (slopes of LMMs)
562 for each bundle (**Fig 2c**).

563 Next, we evaluated the development of R1 along the length of each bundle. For this, we
564 divided each bundle into 100 equidistant nodes and evaluated R1 at each time-point in each node (**Fig**
565 **3**). We then determined the rate of R1 development at each node (one LMM per node; random
566 intercepts for each individual as above). For each bundle, we then plotted R1 measured in newborns
567 and the rate of R1 development across nodes to visualize their relationship along each bundle (**Fig 4**).

568 Finally, we evaluated the relationship between the rate of R1 development (LMM slope) and
569 both the measured R1 in newborns as well as the spatial location in the brain (**Fig 5**). This analysis
570 was done for every 10th node along each bundle to ensure independence across nodes within a bundle.
571 All subplots in **Fig 5** show the data at each node plotted at their average location in the newborn's
572 brain (average $|x|$, y and z coordinates in the newborn sample). For the x axis we used the $|x|$
573 coordinates, as previous work suggests a medial to lateral spatial gradient of development across both
574 hemispheres of the infant brain⁵. As all newborn data was acpc-ed, the (0,0,0) coordinate corresponds
575 to the average coordinate of the anterior commissure across newborns. **Fig 5a** is included to orient

576 the reader to the spatial layout in these plots. **Fig. 5b** shows the spatial layout of measured R1 in
577 newborns across the white matter, and **Fig. 5c** shows the spatial layout of R1 development rate across
578 the white matter.

579 We quantified the relationship between R1 development rate and initial R1 as well as spatial
580 location via a series of LMMs. In these models we used every 10th node of each bundle to ensure
581 independence. In the first LMM, we related R1 development rate to R1 measured in newborns, with
582 a random intercept for each bundle:

583 (1) $R1Slope \sim 1 + R1 \text{ in Newborns} + (1 | \text{Bundle})$.

584 In the second LMM, we related R1 development rate to location in the brain ($|x|$, y , z , $|x|*y$,
585 $y*z$, and $z*|x|$ coordinates, all coordinates were z-scored before including interaction terms), with a
586 random intercept per bundle:

587 (2) $R1Slope \sim 1 + |x| + y + z + |x|*y + |x|*z + y*z + (1 | \text{Bundle})$.

588 In the third model, we related R1 development to both R1 measured in newborns as well as
589 spatial location with a random intercept per bundle:

590 (3) $R1Slope \sim 1 + R1 \text{ in Newborns} + |x| + y + z + |x|*y + |x|*z + y*z + (1 | \text{Bundle})$.

591 We used a likelihood ratio test to assess whether this third model outperforms the second
592 model. Similar LMMs were also performed on mean diffusivity (MD) data, to relate our findings to
593 previous work. MD results are presented in **Supplementary Figs 5-8**.

594

595 **Data and code availability**

596 The data were analyzed using open source software, including mrDiffusion and MRtrix3⁶⁹. We
597 developed a new toolbox for automated fiber quantification in individual infants (babyAFQ) and make
598 it openly available (<https://github.com/yeatmanlab/AFQ/master/babyAFQ>). Code for reproducing

599 all figures is made available in GitHub (<https://github.com/VPNL/babyWmDev>). The data
600 generated in this study will be made available by the corresponding author upon reasonable request.

601

602 **Acknowledgements**

603 The research was funded by: Wu Tsai Neurosciences Institute Big Idea Neurodevelopment
604 Grant, R21 EY030588 grant, and the Center for Mind, Brain and Behavior – CMBB, Philipps-
605 Universität Marburg and Justus-Liebig-Universität Giessen.

606 We would like to thank all participating families, as well as KK Barrows, Amy Kang, Javier
607 Lopez, Laura Villalobos, Nancy Lopez-Alvarez, and Lois Williams for their help with white/gray
608 matter segmentations of infant brains. We would also like to thank Jiyeong Ha for her contributions
609 towards data quality assurance and Caitlyn Estrada for her contribution to data collection.

610

611 **Author contribution**

612 MR, HK, and FRQ collected the data. MR, VN, HK and FRQ generated gray/white matter
613 segmentations and R1 maps. HW developed scanning sequences. MG and JDY developed babyAFQ
614 and data analysis pipeline. MG, JDY and KGS analyzed data. MG and KGS wrote the manuscript. All
615 authors read and edited the manuscript.

616

617 **Competing Interests**

618 The authors declare no competing interests.

619

620 **References**

621 1. Knickmeyer, R. C. *et al.* A structural MRI study of human brain development from birth to 2

- 622 years. *J. Neurosci.* **28**, 12176–12182 (2008).
- 623 2. Flechsig, P. . Anatomie des menschlichen Gehirns und Rückenmarks aus myelogenetischer
624 Grundlage. *JAMA J. Am. Med. Assoc.* **76**, 676 (1921).
- 625 3. Yakovlev, P. I. & Lecours, A.-R. The myelogenetic cycles of regional maturation of the brain.
626 in *Regional Development of Brain in Early Life* 3–70 (1967).
- 627 4. Gilles, F. H., Shankle, W. & Dooling, E. C. MYELINATED TRACTS: GROWTH
628 PATTERNS. in *The Developing Human Brain* 117–183 (Elsevier, 1983). doi:10.1016/b978-0-
629 7236-7017-9.50018-1
- 630 5. Kinney, H. C., Brody, B. A., Kloman, A. S. & Gilles, F. H. Sequence of central nervous
631 system myelination in human infancy: II. Patterns of myelination in autopsied infants. *J.*
632 *Neuropathol. Exp. Neurol.* **47**, 217–234 (1988).
- 633 6. Monje, M. Myelin Plasticity and Nervous System Function. [https://doi-](https://doi-org.stanford.idm.oclc.org/10.1146/annurev-neuro-080317-061853)
634 [org.stanford.idm.oclc.org/10.1146/annurev-neuro-080317-061853](https://doi-org.stanford.idm.oclc.org/10.1146/annurev-neuro-080317-061853) **41**, 61–76 (2018).
- 635 7. Fields, R. D. White matter in learning, cognition and psychiatric disorders. *Trends in*
636 *Neurosciences* **31**, 361–370 (2008).
- 637 8. Dubois, J. *et al.* Exploring the Early Organization and Maturation of Linguistic Pathways in
638 the Human Infant Brain. *Cereb. Cortex* **26**, 2283–2298 (2016).
- 639 9. Deoni, S. C. L. *et al.* Mapping infant brain myelination with magnetic resonance imaging. *J.*
640 *Neurosci.* **31**, 784–791 (2011).
- 641 10. Zatorre, R. J., Fields, R. D. & Johansen-Berg, H. Plasticity in gray and white: Neuroimaging
642 changes in brain structure during learning. *Nat. Neurosci.* **15**, 528–536 (2012).
- 643 11. Gibson, E. M. *et al.* Neuronal activity promotes oligodendrogenesis and adaptive myelination
644 in the mammalian brain. *Science (80-.)*. **344**, (2014).
- 645 12. Hughes, E. G., Orthmann-Murphy, J. L., Langseth, A. J. & Bergles, D. E. Myelin remodeling
646 through experience-dependent oligodendrogenesis in the adult somatosensory cortex. *Nat.*
647 *Neurosci.* **21**, 696–706 (2018).
- 648 13. Makinodan, M., Rosen, K. M., Ito, S. & Corfas, G. A critical period for social experience-
649 dependent oligodendrocyte maturation and myelination. *Science (80-.)*. **337**, 1357–1360 (2012).
- 650 14. Soun, J. E., Liu, M. Z., Cauley, K. A. & Grinband, J. Evaluation of neonatal brain myelination
651 using the T1- and T2-weighted MRI ratio. *J. Magn. Reson. Imaging* **46**, 690–696 (2017).
- 652 15. Deoni, S. C. L., Dean, D. C., O’Muircheartaigh, J., Dirks, H. & Jerskey, B. A. Investigating
653 white matter development in infancy and early childhood using myelin water fraction and
654 relaxation time mapping. *Neuroimage* **63**, 1038–1053 (2012).
- 655 16. Schleicher, A., Amunts, K., Geyer, S., Morosan, P. & Zilles, K. Observer-independent
656 method for microstructural parcellation of cerebral cortex: A quantitative approach to
657 cytoarchitectonics. *Neuroimage* **9**, 165–177 (1999).
- 658 17. Dubois, J. *et al.* The early development of brain white matter: A review of imaging studies in
659 fetuses, newborns and infants. *Neuroscience* **276**, 48–71 (2014).
- 660 18. Dubois, J. *et al.* MRI of the Neonatal Brain: A Review of Methodological Challenges and
661 Neuroscientific Advances. *Journal of Magnetic Resonance Imaging jMRI*.27192 (2020).
662 doi:10.1002/jMRI.27192
- 663 19. Gilmore, J. H., Knickmeyer, R. C. & Gao, W. Imaging structural and functional brain

- 664 development in early childhood. *Nature Reviews Neuroscience* **19**, 123–137 (2018).
- 665 20. Ouyang, M., Dubois, J., Yu, Q., Mukherjee, P. & Huang, H. Delineation of early brain
666 development from fetuses to infants with diffusion MRI and beyond. *NeuroImage* **185**, 836–
667 850 (2019).
- 668 21. Qiu, A., Mori, S. & Miller, M. I. Diffusion tensor imaging for understanding brain
669 development in early life. *Annu. Rev. Psychol.* **66**, 853–876 (2015).
- 670 22. Stephens, R. L. *et al.* White Matter Development from Birth to 6 Years of Age: A
671 Longitudinal Study. *Cereb. Cortex* **00**, 1–17 (2020).
- 672 23. Jones, D. K., Knösche, T. R. & Turner, R. White matter integrity, fiber count, and other
673 fallacies: The do’s and don’ts of diffusion MRI. *NeuroImage* **73**, 239–254 (2013).
- 674 24. Puce, A., Allison, T., Asgari, M., Gore, J. C. & McCarthy, G. Differential Sensitivity of
675 Human Visual Cortex to Faces, Letterstrings, and Textures: A Functional Magnetic
676 Resonance Imaging Study. *J. Neurosci.* (1996). doi:10.1523/JNEUROSCI.16-16-05205.1996
- 677 25. Li, G. *et al.* Computational neuroanatomy of baby brains: A review. *NeuroImage* (2019).
678 doi:10.1016/j.neuroimage.2018.03.042
- 679 26. Mezer, A. *et al.* Quantifying the local tissue volume and composition in individual brains with
680 magnetic resonance imaging. *Nat. Med.* **19**, 1667–1672 (2013).
- 681 27. Edwards, L. J., Kirilina, E., Mohammadi, S. & Weiskopf, N. Microstructural imaging of
682 human neocortex in vivo. *NeuroImage* **182**, 184–206 (2018).
- 683 28. Lutti, A., Dick, F., Sereno, M. I. & Weiskopf, N. Using high-resolution quantitative mapping
684 of R1 as an index of cortical myelination. *Neuroimage* **93**, 176–188 (2014).
- 685 29. Stüber, C. *et al.* Myelin and iron concentration in the human brain: A quantitative study of
686 MRI contrast. *Neuroimage* **93**, 95–106 (2014).
- 687 30. Weiskopf, N., Edwards, L. J., Helms, G., Mohammadi, S. & Kirilina, E. Quantitative
688 magnetic resonance imaging of brain anatomy and in vivo histology. *Nat. Rev. Phys.* 1–19
689 (2021). doi:10.1038/s42254-021-00326-1
- 690 31. Kirilina, E. *et al.* Superficial white matter imaging: Contrast mechanisms and whole-brain in
691 vivo mapping. *Sci. Adv.* (2020). doi:10.1126/sciadv.aaz9281
- 692 32. Yeatman, J. D., Dougherty, R. F., Myall, N. J., Wandell, B. A. & Feldman, H. M. Tract
693 Profiles of White Matter Properties: Automating Fiber-Tract Quantification. *PLoS One* **7**,
694 (2012).
- 695 33. Garyfallidis, E. *et al.* Recognition of white matter bundles using local and global streamline-
696 based registration and clustering. *NeuroImage* **170**, 283–295 (2018).
- 697 34. Kruper, J. *et al.* Evaluating the reliability of human brain white matter tractometry. *bioRxiv*
698 2021.02.24.432740 (2021). doi:10.1101/2021.02.24.432740
- 699 35. Shi, F. *et al.* Infant Brain Atlases from Neonates to 1- and 2-Year-Olds. *PLoS One* **6**, e18746
700 (2011).
- 701 36. Wakana, S. *et al.* Reproducibility of quantitative tractography methods applied to cerebral
702 white matter. *Neuroimage* **36**, 630–644 (2007).
- 703 37. Weiner, K. S., Yeatman, J. D. & Wandell, B. A. The posterior arcuate fasciculus and the
704 vertical occipital fasciculus. *Cortex* (2016). doi:10.1016/j.cortex.2016.03.012
- 705 38. Takemura, H. *et al.* A Major Human White Matter Pathway Between Dorsal and Ventral

- 706 Visual Cortex. *Cereb. Cortex* **26**, 2205–2214 (2016).
- 707 39. Yeatman, J. D. *et al.* The vertical occipital fasciculus: A century of controversy resolved by in
708 vivo measurements. *Proc. Natl. Acad. Sci.* **111**, E5214–E5223 (2014).
- 709 40. Wang, Y. *et al.* Rethinking the role of the middle longitudinal fascicle in language and auditory
710 pathways. *Cereb. Cortex* **23**, 2347–2356 (2013).
- 711 41. Jiang, H. *et al.* Early diagnosis of spastic cerebral palsy in infants with periventricular white
712 matter injury using diffusion tensor imaging. *Am. J. Neuroradiol.* **40**, 162–168 (2019).
- 713 42. Langer, N. *et al.* White Matter Alterations in Infants at Risk for Developmental Dyslexia.
714 *Cereb. Cortex* **27**, 1027–1036 (2017).
- 715 43. Travis, K. E., Adams, J. N., Ben-Shachar, M. & Feldman, H. M. Decreased and increased
716 anisotropy along major cerebral white matter tracts in preterm children and adolescents. *PLoS*
717 *One* **10**, e0142860 (2015).
- 718 44. Yeatman, J. D., Wandell, B. A. & Mezer, A. A. Lifespan maturation and degeneration of
719 human brain white matter. *Nat. Commun.* **5**, 4932 (2014).
- 720 45. Hüppi, P. S. & Dubois, J. Diffusion tensor imaging of brain development. *Semin. Fetal*
721 *Neonatal Med.* **11**, 489–497 (2006).
- 722 46. Dubois, J., Hertz-Pannier, L., Dehaene-Lambertz, G., Cointepas, Y. & Le Bihan, D.
723 Assessment of the early organization and maturation of infants' cerebral white matter fiber
724 bundles: A feasibility study using quantitative diffusion tensor imaging and tractography.
725 *Neuroimage* **30**, 1121–1132 (2006).
- 726 47. Yu, Q. *et al.* Differential White Matter Maturation from Birth to 8 Years of Age. *Cereb. Cortex*
727 **30**, 2673–2689 (2020).
- 728 48. Schneider, J. *et al.* Evolution of T1 relaxation, ADC, and fractional anisotropy during early
729 brain maturation: A serial imaging study on preterm infants. *Am. J. Neuroradiol.* **37**, 155–162
730 (2016).
- 731 49. Grotheer, M., Zhen, Z., Lerma-Usabiaga, G. & Grill-Spector, K. Separate lanes for adding
732 and reading in the white matter highways of the human brain. *Nat. Commun.* **10**, 420216
733 (2019).
- 734 50. Eminian, S., Hajdu, S. D., Meuli, R. A., Maeder, P. & Hagmann, P. Rapid high resolution T1
735 mapping as a marker of brain development: Normative ranges in key regions of interest.
736 *PLoS One* **13**, e0198250 (2018).
- 737 51. Chevalier, N. *et al.* Myelination is associated with processing speed in early childhood:
738 Preliminary insights. *PLoS One* **10**, e0139897 (2015).
- 739 52. Deoni, S. C. L. *et al.* White matter maturation profiles through early childhood predict general
740 cognitive ability. *Brain Struct. Funct.* **221**, 1189–1203 (2016).
- 741 53. Howell, B. R. *et al.* The UNC/UMN Baby Connectome Project (BCP): An overview of the study design
742 and protocol development. *NeuroImage* **185**, 891–905 (2019).
- 743 54. O'Muircheartaigh, J. *et al.* Modelling brain development to detect white matter injury in term
744 and preterm born neonates. *Brain* **143**, 467–479 (2020).
- 745 55. Dubner, S. E., Rose, J., Bruckert, L., Feldman, H. M. & Travis, K. E. Neonatal white matter
746 tract microstructure and 2-year language outcomes after preterm birth. *NeuroImage Clin.* **28**,
747 102446 (2020).

- 748 56. Parikh, N. A., Hershey, A. & Altaye, M. Early Detection of Cerebral Palsy Using
749 Sensorimotor Tract Biomarkers in Very Preterm Infants. *Pediatr. Neurol.* **98**, 53–60 (2019).
- 750 57. Ghazi Sherbaf, F., Aarabi, M. H., Hosein Yazdi, M. & Haghshomar, M. White matter
751 microstructure in fetal alcohol spectrum disorders: A systematic review of diffusion tensor
752 imaging studies. *Human Brain Mapping* **40**, 1017–1036 (2019).
- 753 58. Herskind, A., Greisen, G. & Nielsen, J. B. Early identification and intervention in cerebral
754 palsy. *Dev. Med. Child Neurol.* **57**, 29–36 (2015).
- 755 59. Rosenke, M. *et al.* Myelin contributes to microstructural growth in human sensory cortex
756 during early infancy. *bioRxiv* 2021.03.16.435703 (2021). doi:10.1101/2021.03.16.435703
- 757 60. Smith, R. E., Tournier, J. D., Calamante, F. & Connelly, A. Anatomically-constrained
758 tractography: Improved diffusion MRI streamlines tractography through effective use of
759 anatomical information. *Neuroimage* **62**, 1924–1938 (2012).
- 760 61. Zöllei, L., Iglesias, J. E., Ou, Y., Grant, P. E. & Fischl, B. Infant FreeSurfer: An automated
761 segmentation and surface extraction pipeline for T1-weighted neuroimaging data of infants
762 0–2 years. *Neuroimage* **218**, 116946 (2020).
- 763 62. Li, G. *et al.* Construction of 4D high-definition cortical surface atlases of infants: Methods
764 and applications. *Med. Image Anal.* **25**, 22–36 (2015).
- 765 63. Li, G. *et al.* Measuring the dynamic longitudinal cortex development in infants by
766 reconstruction of temporally consistent cortical surfaces. *Neuroimage* **90**, 266–279 (2014).
- 767 64. Wang, L. *et al.* Volume-based analysis of 6-month-old infant brain MRI for autism biomarker
768 identification and early diagnosis. in *Lecture Notes in Computer Science (including subseries Lecture*
769 *Notes in Artificial Intelligence and Lecture Notes in Bioinformatics)* **11072 LNCS**, 411–419 (Springer
770 Verlag, 2018).
- 771 65. Wu H, Dougherty RF, Kerr AB, Zhu K, Middione MJ, M. A. Fast T1 mapping using slice-
772 shuffled Simultaneous Multi-Slice inversion recovery EPI. *21st Annu. Meet. Organ. Hum. Brain*
773 *Mapp.* (2015).
- 774 66. Moré, J. J. The Levenberg-Marquardt algorithm: Implementation and theory. in 105–116
775 (Springer, Berlin, Heidelberg, 1978). doi:10.1007/bfb0067700
- 776 67. Pietsch, M. *et al.* A framework for multi-component analysis of diffusion MRI data over the
777 neonatal period. *Neuroimage* **186**, 321–337 (2019).
- 778 68. Bastiani, M. *et al.* Automated processing pipeline for neonatal diffusion MRI in the
779 developing Human Connectome Project. *Neuroimage* **185**, 750–763 (2019).
- 780 69. Tournier, J. D. *et al.* MRtrix3: A fast, flexible and open software framework for medical image
781 processing and visualisation. *bioRxiv* **202**, 551739 (2019).
- 782 70. Tournier, J. D., Calamante, F. & Connelly, A. MRtrix: Diffusion tractography in crossing
783 fiber regions. *Int. J. Imaging Syst. Technol.* **22**, 53–66 (2012).
- 784 71. Veraart, J. *et al.* Denoising of diffusion MRI using random matrix theory. *Neuroimage* **142**,
785 394–406 (2016).
- 786 72. Andersson, J. L. R., Graham, M. S., Zsoldos, E. & Sotiropoulos, S. N. Incorporating outlier
787 detection and replacement into a non-parametric framework for movement and distortion
788 correction of diffusion MR images. *Neuroimage* **141**, 556–572 (2016).
- 789 73. Tustison, N. J. *et al.* N4ITK: Improved N3 bias correction. *IEEE Trans. Med. Imaging* **29**,
790 1310–1320 (2010).

- 791 74. Dhollander, T., Raffelt, D. & Connelly, A. Unsupervised 3-tissue response function
792 estimation from single-shell or multi-shell diffusion MR data without a co-registered T1
793 image. in *ISMRM Workshop on Breaking the Barriers of Diffusion MRI 5* (2016).
- 794 75. Jeurissen, B., Tournier, J. D., Dhollander, T., Connelly, A. & Sijbers, J. Multi-tissue
795 constrained spherical deconvolution for improved analysis of multi-shell diffusion MRI data.
796 *Neuroimage* **103**, 411–426 (2014).
- 797 76. Dice, L. R. Measures of the Amount of Ecologic Association Between Species. *Ecology* **26**,
798 297–302 (1945).
- 799
- 800